



# Oxygen isotope constraints on the ventilation of the modern and glacial Pacific

Bruno Millet<sup>1</sup> · William R. Gray<sup>1</sup> · Casimir de Lavergne<sup>2</sup> · Didier M. Roche<sup>1,3</sup>

Received: 9 May 2023 / Accepted: 29 July 2023 / Published online: 31 August 2023  
© The Author(s) 2023

## Abstract

Changes in Pacific tracer reservoirs and transports are thought to be central to the regulation of atmospheric CO<sub>2</sub> on glacial–interglacial timescales. However, there are currently two contrasting views of the circulation of the modern Pacific; the classical view sees southern sourced abyssal waters upwelling to about 1.5 km depth before flowing southward, whereas the bathymetrically constrained view sees the mid-depths (1–2.5 km) largely isolated from the global overturning circulation and predominantly ventilated by diffusion. Furthermore, changes in the circulation of the Pacific under differing climate states remain poorly understood. Through both a modern and a Last Glacial Maximum (LGM) analysis focusing on oxygen isotopes in seawater and benthic foraminifera as conservative tracers, we show that isopycnal diffusion strongly influences the mid-depths of the Pacific. Diapycnal diffusion is most prominent in the subarctic Pacific, where an important return path of abyssal tracers to the surface is identified in the modern state. At the LGM we infer an expansion of North Pacific Intermediate Water, as well as increased layering of the deeper North Pacific which would weaken the return path of abyssal tracers. These proposed changes imply a likely increase in ocean carbon storage within the deep Pacific during the LGM relative to the Holocene.

**Keywords** Pacific Ocean · Ocean circulation · Ventilation · Oxygen isotopes · Last Glacial Maximum

## 1 Introduction

Atmospheric CO<sub>2</sub> varied by up to 100 ppm over glacial–interglacial cycles and is closely linked to changes in global temperature (Augustin et al. 2004). Understanding the

mechanisms underpinning these variations in atmospheric CO<sub>2</sub> may help us to understand key carbon cycle feedbacks within the climate system relevant for future climate change. Because of its size and the timescale at which it can interact with the atmosphere, the deep ocean is the most likely candidate to store and release carbon over glacial–interglacial cycles (Sigman and Boyle 2000; Adkins 2013). The Pacific represents about 50% of the global ocean volume and contains the oldest and most carbon-rich waters in the global ocean (Key 2004). Yet, despite being fundamental to our understanding of the carbon cycle, the circulation of the Pacific in the modern climate—and, by extension, in past climates—remains poorly understood (e.g. Stewart 2017; Hautala 2018; Kawasaki et al. 2021). The role of the Pacific ocean in the global carbon cycle, and inferred glacial–interglacial changes in Pacific upper-ocean circulation (Keigwin 1998; Matsumoto et al. 2002; Okazaki et al. 2010; Rae et al. 2014, 2020; Struve et al. 2022), motivate further inquiry into Pacific tracer distributions.

The global overturning circulation ventilates the deep ocean through the formation and sinking of dense waters at high latitudes of the North Atlantic and Southern Ocean.

---

✉ Bruno Millet  
bruno.millet@lsce.ipsl.fr

William R. Gray  
william.gray@lsce.ipsl.fr

Casimir de Lavergne  
casimir.delavergne@locean.ipsl.fr

Didier M. Roche  
didier.roche@lsce.ipsl.fr

<sup>1</sup> Laboratoire des Sciences du Climat et de l'Environnement, LSCE/IPSIL, CEA-CNRS-UVSQ, Université Paris-Saclay, Orme des Merisiers, 91191 Gif-sur-Yvette, France

<sup>2</sup> LOCEAN Laboratory, Sorbonne Université-CNRS-IRD-MNH, 4 place Jussieu, 75005 Paris, France

<sup>3</sup> Faculty of Science, Department of Earth Sciences, Vrije Universiteit Amsterdam, Amsterdam, The Netherlands

The newly formed waters progressively replace older deep waters and thereby flush carbon sequestered by the biological pump back to the upper ocean and atmosphere. As the North Pacific is remote from the main sources of deep water formation, its waters deeper than 1 km are very old, depleted in oxygen and enriched in carbon (Key 2004). Characterizing the mechanisms by which the North Pacific is slowly ventilated is therefore crucial to our understanding of oceanic carbon storage.

In the modern Pacific below the main thermocline, ventilation is thought to occur via three main circulation branches (Fig. 1). At intermediate depths, down to about 1 km, Antarctic Intermediate Water (AAIW) formed in the Southern Ocean dominates ventilation of the South Pacific, while North Pacific Intermediate Water (NPIW) formed in the northwest end of the basin dominates ventilation of the North Pacific. In deeper layers, ventilation relies exclusively on waters coming from the Southern Ocean, since there is no formation of deep water in the North Pacific (Warren 1983). The drivers and pathways of this deep ventilation remain debated (Holzer et al. 2021). Indeed, there are two contrasting views of the deep Pacific circulation, illustrated in Fig. 1, that disagree on the ventilation of the mid-depths. Talley (2013) described dense Antarctic waters (AABW) flowing northward deeper than about 3.5 km, before they upwell diffusively up to about 1.5 km depth, and return southward as Pacific Deep Water (PDW) to the Southern Ocean surface. An alternative view (de Lavergne et al. 2017) contends that the bulk of diffusive upwelling is confined to abyssal depths where the seafloor is abundant, leaving a mid-depth layer that is excluded from the overturning and weakly ventilated by diffusion and recirculation. This latter 'bathymetrically constrained' circulation is supported by

estimates of water mass transformation by tidal mixing and geothermal heating (de Lavergne et al. 2022; Kawasaki et al. 2021), and is qualitatively consistent with observed silicate and radiocarbon distributions (de Lavergne et al. 2017) as well as inverse modelling of multiple geochemical tracers (Holzer et al. 2021).

Multiple lines of evidence indicate changes in deep ocean circulation between the LGM and Holocene. Although still subject of debate, proposed alterations at LGM relative to today include a shallower northern component of deep water formed in the North Atlantic (Curry and Oppo 2005; Ferrari et al. 2014), an enhanced NPIW source (e.g. Keigwin 1998; Matsumoto et al. 2002; Rae et al. 2020), and a colder and saltier global ocean, with enhanced deep stratification due to salinity rather than temperature (Adkins et al. 2002). On the other hand, the abyssal overturning cell could be expected to have a broadly unaltered structure, set by deep topography (Toggweiler and Samuels 1995a; de Lavergne et al. 2017).

In order to shed light on both modern and past physical ocean states, we use conservative tracers. We first explore ventilation pathways in the modern Pacific by using temperature, salinity, the oxygen isotopic ratio of seawater and preformed phosphate. Then, we investigate changes in ventilation during the LGM with the oxygen isotopic ratio within  $\text{CaCO}_3$  shells of benthic foraminifera *Cibicidoides mundulus*, *Cibicidoides wuellerstorfi* and *Planulina spp.* Those three genus are closely related and equally reliable; their isotopic ratio acts as a quasi-conservative tracer (Lund et al. 2011). We find that the mid-depths of both the modern and LGM Pacific host tracer extrema that cannot result from a mixture of waters above and below. This pattern is consistent with a vertically compressed abyssal overturning and a prominent influence of isopycnal diffusion on

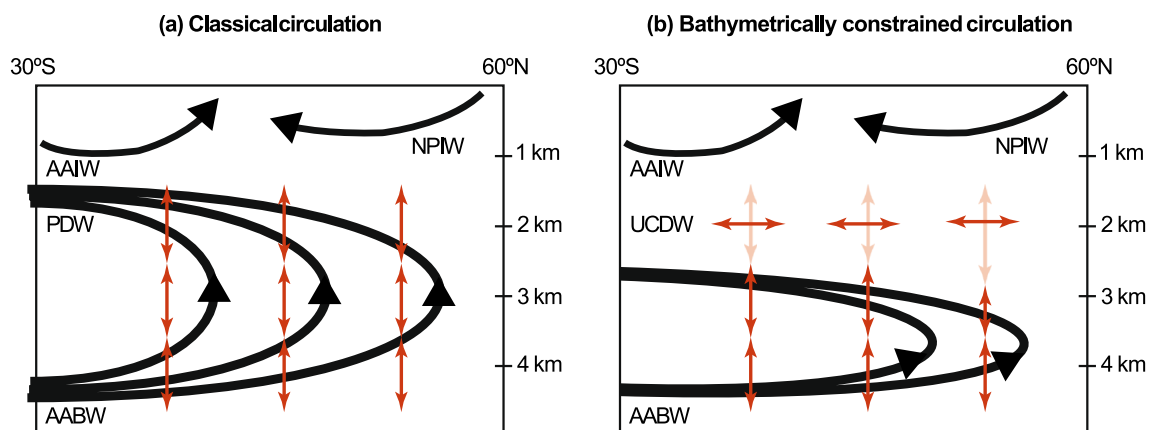


**Fig. 1** Two distinct views of the modern Pacific deep circulation, adapted from Holzer et al. (2021). The classical overturning circulation is sketched in (a), the bathymetrically constrained circulation in (b). Thick black curves illustrate major branches of the overturning circulation. Double-headed vertical and horizontal red arrows illus-

trate respectively vertical mixing and isopycnal mixing. Prominent water masses are labeled: Antarctic Bottom Water (AABW), Pacific Deep Water (PDW), Upper Circumpolar Deep Water (UCDW), Antarctic Intermediate Water (AAIW) and North Pacific Intermediate Water (NPIW)

Pacific mid-depth waters. However we also find evidence of upwelling of abyssal tracers in the modern subarctic Pacific. At the LGM, this upwelling may have been suppressed, while NPIW formation was enhanced.

## 2 Least-squares method

In order to characterise ventilation patterns in the modern Pacific, we developed a least-squares method to estimate the fractional contribution of four end-members (corresponding to the water masses labeled in Fig. 1) to local water volumes. The resultant distributions of water fractions give a simple integrated view of circulation and mixing (see e.g. Johnson 2008; Rae and Broecker 2018). We describe in turn the tracers that we use in our modern study, the least-squares calculation and the definition of the end-members.

### 2.1 Conservative tracers for the modern ocean

In this study, we focus on conservative tracers, that is, tracers that have no sources and sinks away from ocean boundaries. In the ocean interior, such tracers only change due to advection and diffusion, so that their distributions bear direct information on ocean circulation and mixing. The four chosen tracers are shown as a zonal average over the main Pacific basin in Fig. 2. Note that the 'main Pacific' (see Fig. 2a) refers to the Pacific excluding semi-enclosed seas and waters east of the East Pacific Rise, following de Lavergne et al. (2017).

First, we calculated conservative temperature ( $\Theta$ ) and preformed salinity ( $S$ ) using the Gibbs SeaWater toolbox of McDougall and Barker (201) and the WOCE global hydrographic climatology of Gouretski and Koltermann (2004), an annual mean climatology constructed using along-isopycnal interpolation. Preformed salinity is closely related to absolute salinity but excludes biological contributions to salinity, and in particular excludes the contribution of silicate which is significant in the deep Pacific (McDougall et al. 2012).

Next, we attempted to remove the impact of geothermal heating on temperatures of the deep Pacific, since this heat source along the seafloor could bias our estimates of water fractions which assume strict tracer conservation throughout the deep Pacific north of 30°S. We decided to approximate and remove the geothermal heating effect using a simple linear function of depth which increases from 0 °C at 1 km to 0.5 °C at 6 km depth, which we subtract from the three-dimensional conservative temperature field. This linear vertical profile finds justification in the model analysis of Emile-Geay and Madec (2009) (see their Figure 6c). We note that this correction has little impact on our results: it changes the estimated AABW fractions

in the abyss by at most a few percent, while reducing the overall error of the method (see Sect. 2.4).

Preformed phosphate,  $PO_4^*$ , defined by Broecker et al. (1985), was calculated from the GLODAPv2 product (Olsen et al. 2016), using a phosphate to oxygen ratio of 1:175 following Rae and Broecker (2018). This tracer is approximately conserved in the deep ocean, because the oxygen consumed in the remineralization of organic matter is broadly constant in the deep ocean (Anderson and Sarmiento 1994). Like conservative temperature and preformed salinity,  $PO_4^*$  displays a clear vertical gradient between the abyss and the mid-depths, with higher  $PO_4^*$  values in the abyss (Fig. 2b). While latitudinal variations in the C:P ratio of organic matter (Moreno et al. 2022) may lead to non-conservative spatial bias in  $PO_4^*$ , these deviations from Redfield stoichiometry cannot explain the depth structure we observe.

The seawater oxygen isotope ( $\delta^{18}O_{sw}$ ) climatology used is the gridded product of LeGrande and Schmidt (2006). The zonal average of  $\delta^{18}O_{sw}$  in the main Pacific exhibits a mid-depth maximum throughout the basin (Fig. 2c). It must be emphasized that seawater  $\delta^{18}O$  measurements contributing to the climatology are extremely scarce in the deep Pacific. However, the mid-depth maximum appears to be a robust feature, not an artefact of the mapping, as it is present in several individual datasets (e.g. Herguera et al. 1992; Keigwin 1998; McCave et al. 2008). This maximum cannot be explained by vertical mixing and upwelling of AABW: it must originate from lateral (diffusive and/or advective) transport from the Southern Ocean. Although  $\delta^{18}O_{sw}$  is conservative, a clear discontinuity is observable around 20°N in Fig. 2c; this artefact stems from the region-by-region gridding procedure of LeGrande and Schmidt (2006). The employed climatology of  $\delta^{18}O_{sw}$  is thus imperfect, and increasing the spatial coverage and inter-calibration of  $\delta^{18}O_{sw}$  data in the Pacific will help to further constrain ventilation patterns.

The spatial structure of  $\delta^{18}O_{sw}$  suggests a dominant south-to-north transport of this tracer at mid-depths in the Pacific, which would support the circulation regime presented in Fig. 1b.

In order to quantitatively assess the constraints on Pacific ventilation contained in our four tracer distributions, we develop a least-squares algorithm that quantifies the volume contributions of each water mass in the Pacific, using AABW, AAIW, NPIW and either PDW [as a representation of the classical circulation] or Upper Circumpolar Deep Water (UCDW) [as a representation of the bathymetrically constrained circulation] as our end-members. We will show that the calculation is most accurate when the fourth end-member is defined as 30°S UCDW (see Sect. 3).

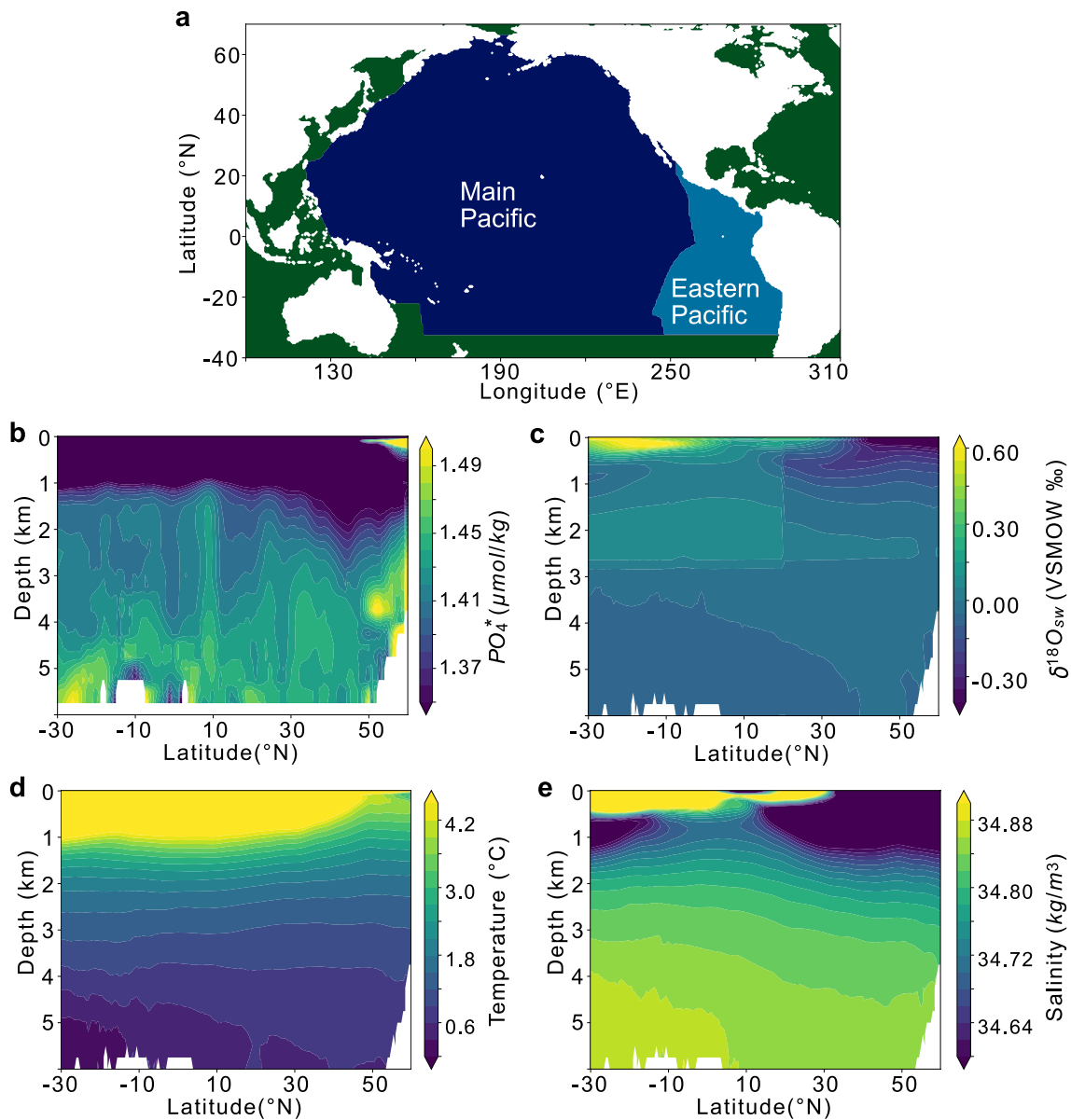


**Fig. 2** (a) Shows the mask that defines the 'main Pacific' domain, which excludes the semi-enclosed seas and waters east of the East Pacific Rise, following de Lavergne et al. (2017). Zonal averages over the 'main Pacific' of the four tracers used in the least-squares method are plotted in (b–e). Preformed phosphate (b) is defined following Rae and Broecker (2018) and computed using GLODAPv2 gridded

fields (Olsen et al. 2016). The oxygen isotopic ratio of seawater (c) is based on the gridded field of LeGrande and Schmidt (2006). Conservative temperature corrected from geothermal heating (d), and preformed salinity (e), are based on the WOCE global hydrographic climatology (Gouretski and Koltermann 2004)

## 2.2 Water fractions algorithm

The water-fraction algorithm is an optimization problem based on four conservative tracers:  $\Theta$ ,  $S$ ,  $\delta^{18}O_{sw}$  and  $PO_4^*$ . The optimization problem uses a linear least squares method to approximate, at each point of our grid (45 depth levels,  $0.5^{\circ} \times 0.5^{\circ}$  horizontal resolution), the four water fractions. These fractions represent the contribution of each end-member to the volume (hence tracer content) of each grid cell.

The water fractions are obtained by minimizing the resultant  $r$  based on the following equation:

$$\|Mf - d\|^2 = r^2 \quad (1)$$

Our optimization variable is a (1, 4) vector,  $f$ , representing the fractions of our four end-members,  $d$  is a (1, 5) vector containing the physical and biochemical properties of the ocean at this grid-point.  $M$  is a (5, 4) matrix that contains

the values of the end-member for each tracer divided by the typical range of the tracer in the deep Pacific. Dividing the tracer values by their typical variation is necessary when we sum and compare each tracer error in order to minimize the total error of the method. Typical variations are defined as follows: we average horizontally each tracer over the whole deep ( $\geq 1$  km) Pacific, and take the largest difference in the resulting vertical profile. The obtained values are referenced in Table 1. The fifth parameter entering the minimization, corresponding to the fifth row in the left-hand-side of Eq. (1), ensures that the sum of our fractions is very close to 1. Furthermore, a constraint is placed on the fractions such that they are comprised between 0 and 1. Our problem is thus over-constrained and we could add new end-members should we desire to.

Although all conservative, our tracers are not equally reliable. Thus we associate weights to control the relative influence of each tracer in our optimization problem, therefore in  $M$  and  $d$ . Following Johnson (2008), we decided to put the relative weight of temperature at one-fourth the weight of salinity. Subjectively, we set the weight of  $\delta^{18}\text{O}_{sw}$  at a quarter of that of temperature because the data for the deep Pacific is very scarce, and because of artefacts in the interpolation. The weight of  $\text{PO}_4^*$  is chosen to be one-half the weight of temperature because this tracer is reconstructed from two biochemical tracers that are less well observed than temperature and salinity and because of the required assumptions in the Redfield stoichiometry. Although the exact choice of weights is subjective, we found that changing them over reasonable ranges did not alter the broad structure that we identify.

### 2.3 Definition of the end-members

The AAIW, UCDW and AABW end-members are defined at  $30^\circ\text{S}$  by averaging over specific neutral density ( $\gamma^n$ ) (see Jackett and McDougall 1997) ranges, that are characteristic of each water mass according to previous studies and our

**Table 1** This table lists the tracer values of each end-member used for our water fractions algorithm

	$\Theta$ ( $^\circ\text{C}$ )	S ( $\text{kg m}^{-3}$ )	$\delta^{18}\text{O}_{sw}$ (‰)	$\text{PO}_4^*$ ( $\mu\text{ mol kg}^{-1}$ )
AABW	0.435	34.868	-0.0572	1.435
UCDW	2.342	34.746	0.0515	1.417
AAIW	4.771	34.511	-0.0527	1.283
NPIW	6.438	34.130	-0.227	0.872
Typical variations	3.456	0.229	0.114	0.102
Weight	1	4	0.25	0.5
Error max	1.728	0.0287	0.227	0.102

The typical range, weight and maximum tolerated error of each tracer are also given

inspection of  $30^\circ\text{S}$  tracer distributions. The UCDW end-member tracer values are averages between 27.7 and 27.95 neutral density surfaces. Although UCDW is usually defined as the 27.5–28 neutral density range in the Southern Ocean, we reduced the range to minimise overlap with AAIW in the South Pacific. Indeed, the AAIW end-member is defined as the water between the 27.2 and 27.5 neutral density surfaces, at  $30^\circ\text{S}$ . The AABW end-member is taken to be the water below the 28.11 neutral density surface at  $30^\circ\text{S}$  (Ganachaud and Wunsch 2000; de Lavergne et al. 2017). For the NPIW end-member, we choose a specific location in the North Pacific to determine the NPIW, following Johnson (2008):  $37^\circ\text{N}$ ,  $159.5^\circ\text{E}$  and 400 m depth. The neutral density there is 26.8, well within the typical density range of NPIW ( $\sim 26.7$ – $26.9$ ) (Talley 1993). The four end-member values for each tracer are reported in Table 1.

The definition of PDW is somewhat more ambiguous, as PDW is usually interpreted as the product of distributed upwelling and transformation of AABW, enabled by vertical mixing. The large degree of transformation, apparent in the observed vertical tracer gradients between 5 and 1.5 km in Fig. 2, motivates the inclusion of a PDW end-member distinct from AABW. For a fair comparison to the  $30^\circ\text{S}$  UCDW end-member scenario, we try multiple definitions of the PDW end-member: tracer values are averaged over the main Pacific basin for a neutral density of  $\gamma_n = 27.8 \text{ kg m}^{-3}$  (as defined by Talley 2013) at different latitudes:  $20^\circ\text{S}$ ,  $0^\circ\text{N}$ ,  $20^\circ\text{N}$  or  $40^\circ\text{N}$ , giving four different scenarios. In a fifth scenario the PDW end-member tracer values are volume averaged at the same density and over the  $20^\circ\text{S}$ – $40^\circ\text{N}$  range within the main Pacific basin.

### 2.4 Error discrimination

This model aims to broadly represent deep ventilation patterns, and we cannot expect it to capture all features of the Pacific hydrography. In particular the model will fail in low-latitude upper-ocean waters since it lacks appropriate end-members there. We therefore introduce an error threshold beyond which we mask out the output of our optimization problem. Specifically, the water fractions estimated by the algorithm allow to reconstruct local tracer values from the end-member values. If the difference between the reconstructed and actual tracer values is too large then we determine that our model is unable to explain how the ocean is ventilated at this specific location.

The error is calculated as the norm of our resultant  $r$ , representing the deviations between our predictions and the actual values of the tracers. We define a threshold above which the results will be considered erroneous. This threshold implies a maximum tolerated error for each tracer, given in Table 1. Note that this maximum is never reached because



errors beyond the threshold are due to several tracers rather than a single one.

### 3 Water fraction estimates in the modern Pacific

We first compare six simulations with different choices for the fourth end-member (Table 2). We define the total error of a simulation as the sum of resultants over all grid points of the main Pacific at depths greater than 500 m. This error is a measure of the ability of obtained water fractions to reconstruct three-dimensional tracer distributions across the considered Pacific domain. We find that the error decreases as the PDW end-member is moved toward the south, and is smallest using the 30°S UCDW end-member (Table 2). Hence, the optimization works best when the mid-depth end-member is defined at the southern boundary of the domain,

**Table 2** This table reports a measure of total error for each simulation, where the error is normalized by that of our reference simulation (using the UCDW end-member defined at 30°S)

PDW ( $\gamma_n = 27.8$ )	- 20°N	0°N	20°N	40°N	- 20 to 40°N
Error normalized to UCDW	1.02	1.04	1.16	1.45	1.08

Only the fourth end-member (UCDW or PDW) definition changes across simulations, and the error associated to each simulation is shown (with the error associated to the UCDW being 1)

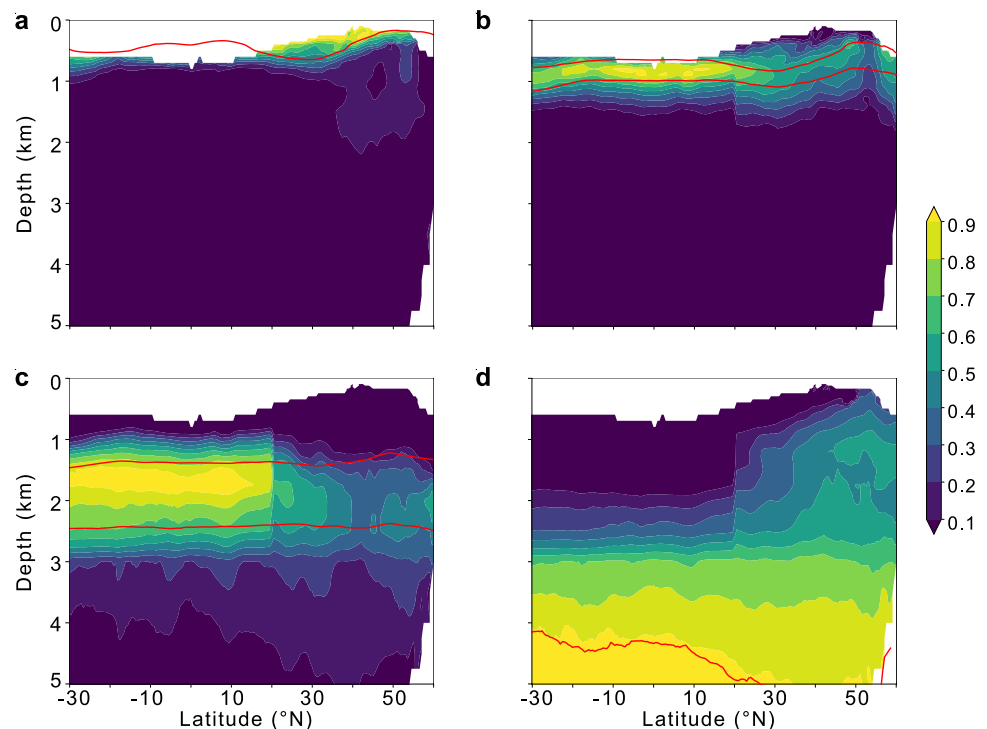
rather than inside the domain. This result, not obvious since one could expect a more central end-member to yield a better average match with tracer observations, suggests that the preferential ventilation pathway of Pacific mid-depths is south-to-north. Interestingly, the simulation in which the PDW end-member is defined at 40°N creates a very local water mass (see Supplementary Figure S1), suggesting that the water at this location is a fairly stagnant and unique mixture of the surrounding sources.

In all the following, we only retain the scenario with the UCDW end-member, and we will use the phrase 'dominating fraction' when a fraction is superior to the sum of the other three. The results are illustrated in Fig. 3, where zonally averaged fractions are shaded and the characteristic isopycnals of each water mass are drawn in red.

The fractions indicate that the mid-depths (1–3 km) of the Pacific, up to 35°N, exhibit tracer distributions that are compatible with ventilation dominantly through isopycnal diffusion from the south. The zonal mean UCDW fraction is above 0.7 between 1.5 and 2.5 km depth up to 20°N (Fig. 3c). The UCDW mid-depth tongue erodes further north, until it is no longer the dominating fraction, around 35°N.

The AABW end-member dominates below 3 km depth, and almost throughout the water column of the subarctic Pacific, north of 45°N, as shown by Fig. 3d. The latter feature suggests the upwelling of abyssal tracers there. Diffusive (and possibly advective) upwelling in the subarctic Pacific was identified in radiocarbon observations (Toggweiler et al.

**Fig. 3** This figure illustrates water fractions from our reference simulation (using UCDW as the fourth end-member). Each fraction is zonally averaged over the main Pacific basin, as defined in Fig. 2a. Characteristic isopycnals of each end-member are overlain in red. The NPIW fraction (a) is mainly situated above the 26.9 neutral density surface, and confined to the North Pacific. The AAIW (b) and UCDW (c) fractions are mainly enclosed by their end-member density range, respectively 27.2–27.5 and 27.7–27.95. The AABW fraction (d) is at its highest below the 28.11 neutral density surface, and is dominant in the major part of the Pacific ocean below 3 km



2019) and a data-constrained inverse model of ocean circulation (Holzer et al. 2021). Additionally, advective upwelling of deep water is deemed necessary in the formation of the modern NPIW (Warren 1983). Whether advective or diffusive, the upwelling probably occurs along topography in the northernmost Pacific, with its signature spreading southward (to about 30°N, Fig. 3d) through isopycnal diffusion and recirculation.

The NPIW fraction is mainly confined to the intermediate depths of the North Pacific, dominating within 200–800 m and 10–50°N (Fig. 3a). NPIW fractions above 0.1 are found down to about 2 km depth north of 30°N, suggesting weak downward diffusion of NPIW tracers to that depth. In accord with Sarmiento et al. (2004), the NPIW core underlies the entire North Pacific subtropical gyre. Finally, the AAIW fraction dominates near 1 km depth in both the South and North Pacific (Fig. 3b). The upward shift north of 30°N follows the sloping isopycnals of the North Pacific subpolar gyre.

The abrupt transition at 20°N in the values of UCDW and AABW fractions that we obtain is due to the discontinuity in the  $\delta^{18}\text{O}_{\text{sw}}$  product. However the transition also reflects a real (smoother) feature because the UCDW fraction remains relatively high up to 35°N and only there becomes outmatched by AABW. In addition, a simulation with only temperature and salinity tracers and only three end-members (removing either AAIW or NPIW) yields about the same result (Supplementary Figure S2). This shows that the northward reduction in the UCDW fraction at mid-depths is not an artifact of the  $\delta^{18}\text{O}_{\text{sw}}$  discontinuity but a real feature.

## 4 Glacial profile of $\delta^{18}\text{O}_{\text{CaCO}_3}$ and its implications for circulation

### 4.1 Changes in $\delta^{18}\text{O}_{\text{CaCO}_3}$ between the LGM and Holocene

In order to investigate changes in circulation at the LGM we use the  $\delta^{18}\text{O}_{\text{CaCO}_3}$  ( $\delta_c$ ) of *Cibicidoides* & *Planulina*.  $\delta_c$  is a function of  $\delta^{18}\text{O}_{\text{sw}}$  and in-situ temperature, hence it is approximately conservative (Lund et al. 2011). The only non-conservative variations of  $\delta_c$  arise due to the moderate increase of in-situ temperature with pressure; an effect that can be estimated and corrected for (Marchitto et al. 2014).

We compiled the sediment core data from three different studies (Keigwin 1998; Matsumoto et al. 2002; Herguera et al. 2010) (see Fig. 4a) that provide water column profiles of  $\delta_c$  from the North Pacific. These datasets provide a sparse sampling of the basin from 20°N up to 55°N, and from the coast of Japan to that of Baja California. The Holocene and

LGM  $\delta_c$  measurements from these cores are shown as a function of depth in Fig. 4c. In order to help identify the trends with depth, we fit both the Holocene and LGM data with a generalised additive model (GAM) (Wood 2011), with the smoothing term determined by restricted maximum likelihood (REML) (Wood et al. 2016). The resultant Holocene  $\delta_c$  profile is relatively uniform below 2 km depth, consistent with the near-uniform distributions of temperature and  $\delta^{18}\text{O}_{\text{sw}}$  at these depths of the modern North Pacific (Fig. 2c,d). By contrast, the glacial  $\delta_c$  profile exhibits a maximum centred near 2.5–3 km depth. The maximum is visible in both of the individual datasets that span this depth range (Keigwin 1998; Matsumoto et al. 2002), indicating that it is a robust feature in the data and not an artifact of inter-laboratory offsets. This maximum cannot be explained by the pressure dependence of in-situ temperature, which could account for a decrease of only 0.025 per mil in  $\delta_c$  between 4 and 3 km depth (0.1 °C). The maximum can neither come from vertical advective-diffusive transport of AABW or NPIW, since both water masses have lower  $\delta_c$ . Instead, we hypothesize that this maximum stems from isopycnal diffusion of higher  $\delta_c$  coming from Southern Ocean mid-depths.

The  $\delta_c$  gradient between intermediate and mid-depths is also stronger in the glacial profile than in the Holocene profile (Fig. 4b). This difference may be explained by a glacial expansion of NPIW, whose influence likely reached deeper down than today (e.g. Keigwin 1998; Matsumoto et al. 2002; Rae et al. 2020).

Next, we assess whether these two major changes in the  $\delta_c$  profile between the LGM and the Holocene can be explained by a change in the end-member tracer values, or whether they imply a change in water fractions (i.e., a change in circulation and mixing).

### 4.2 Attributing profile changes

Before discussing potential drivers of the change in  $\delta_c$  profile, we first consider the differences in the spatial sampling of tracer fields between modern and LGM states; whereas 3-D gridded tracer climatologies are available to us in the modern, we rely on sparse observations at the LGM ( $n = 59$  cores). To test if the spatial sampling of the sediment cores can be considered representative of the wider North Pacific we sample the 3-D fields of modern tracers and water fractions at the sediment core locations, and compare the resulting profiles to the basin (20–55°N) averages (Supplementary Figures S3 and S4). This comparison indicates that our compilation can indeed represent the broad-scale hydrographic features of the North Pacific deeper than 1.7 km. At shallower depths, tracers contain more pronounced horizontal variability: for example, relatively cold waters occupy the

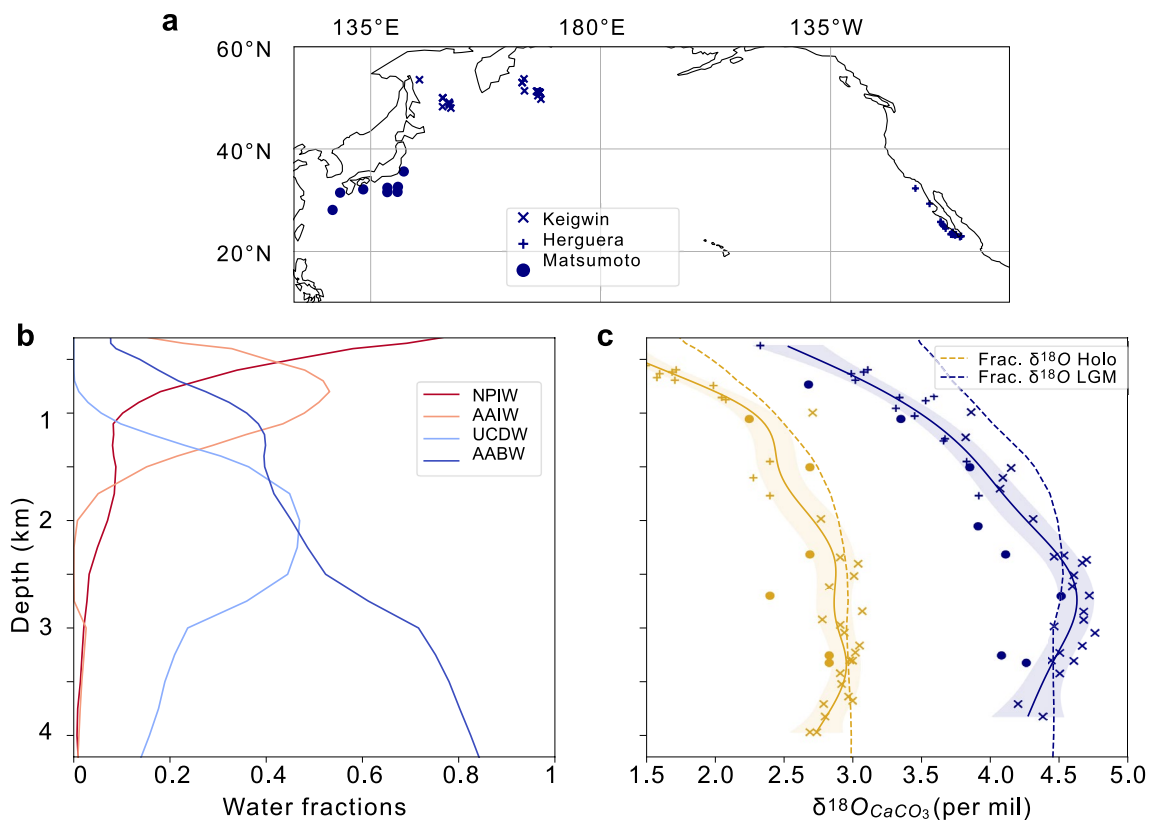


**Fig. 4** (a) Displays the spatial distribution of our compilation of sediment cores. (b) Shows water fractions horizontally averaged between 20°N and 55°N, as estimated here for the modern North Pacific. Red is NPIW, orange is AAIW, light blue is UCDW and navy blue is AABW. (c) Shows the North Pacific  $\delta_c$  data from our compilation of benthic foraminifera as a function of water depth. Time slices for the Late Holocene (yellow) and the LGM (navy blue) were extracted from the different studies. Sediment cores published by Keigwin

(1998) are represented by crosses; the ones from Matsumoto et al. (2002), represented by circles; and the ones from Herguera et al. (2010), represented by plus signs. Both modern and glacial data have been fitted with a GAM (solid curves; 95% confidence interval is shaded). The ice volume effect was not subtracted from the glacial data. Reconstructed  $\delta_c$  profiles from the fractions and appropriate end-member values (see Table 3) are also plotted as dashed curves in (c)

highest latitudes and relatively salty waters run along the eastern boundary. As a result, the intermediate-depth sites of Keigwin (1998) are biased toward AABW whereas those of Herguera et al. (2010) are biased toward AAIW and UCDW (Supplementary Figures S3 and S4). These sampling biases should be borne in mind when interpreting the Holocene data; at LGM, however, intermediate-depth data suggest coherent properties throughout the basin (Fig. 4b), likely due to expanded NPIW influence.

We now assess whether we can reconstruct the modern and glacial  $\delta_c$  profiles with our horizontally-averaged modern water fractions over the North Pacific (Fig. 4b) and appropriate end-member values. This reconstruction thus assumes unchanged water fractions at the LGM relative to today. We denote by  $f_i$  the modern fractions averaged over the North Pacific and by  $\delta_{c,i}$  the value of  $\delta_c$  for each end-member. The reconstructed profile ( $\delta_{c,r}$ ) is then determined at each depth using  $\delta_{c,r} = \sum_i f_i * \delta_{c,i}$

The reconstruction requires end-member values for the LGM, and consistently defined values for the Holocene (Table 3). For the UCDW and AAIW end-members we choose cores around 45°S east of New Zealand (Supplementary Figure S5), an ideal location to capture flow into the Pacific basin (Warren 1973). Finding a core to represent the AABW end-member is difficult because of carbonate dissolution in the deep Pacific and of the scarcity of sufficiently deep cores. Nonetheless, a core near Tasmania exists at a location where the modern neutral density is 28.18 and where modern temperature and salinity are about the same as the AABW end-member values of Table 1; this core is thus chosen for the AABW  $\delta_{c,i}$ . The determination of NPIW  $\delta_{c,i}$  is most ambiguous because we do not know precisely how this water mass evolved during the LGM. We choose to compute the modern NPIW  $\delta_{c,i}$  using the equation from Marchitto et al. (2014) that relates  $\delta_c$  to temperature and  $\delta^{18}O_{sw}$ . For its glacial counterpart, we exploit our GAM fit to the glacial data (shown



**Table 3** Table summarizing the chosen sediment cores and corresponding  $\delta_c$  end-member values employed to reconstruct the North Pacific  $\delta_c$  profile in the modern and glacial states

Water mass	Core	Modern $\gamma_n$	Modern $\delta^{18}\text{O}_{\text{CaCO}_3}$	LGM $\delta^{18}\text{O}_{\text{CaCO}_3}$
AABW	RS147-GC34	28.18	3.01	4.35
UCDW	SO213_2_82-1	27.9	3.00	4.73
NPIW	Computed	26.80	1.55	3.36
AAIW	SO136-003	27.32	2.13	3.91

The modern neutral density ( $\gamma_n$ ) at each site is also given. Only the NPIW end-member values were computed and not deduced from one core, because of the complexity of selecting a representative core for this water mass. The *RS147-GC34* core (147.742°E, 45.1°S, 4002 m deep)  $\delta_c$  values were taken from Moy et al. (2006) while *SO213\_2\_82-1* (176.602°E, -45.778°S, 2066 m deep) and *SO136-003* (169.878°E, 42.296°S, 944 m deep) values come from Ronge et al. (2015)

in Fig. 4c) and take the value at 900 m depth, where glacial NPIW is expected to dominate. The  $\delta_{c,i}$  values selected are referenced in Table 3.

It is noteworthy that the glacial UCDW  $\delta_c$  is higher than its AABW and AAIW counterparts, whereas the Holocene end-member values of AABW and UCDW are almost identical (Table 3). These patterns may be understood by considering the two factors affecting  $\delta_c$ :  $\delta^{18}\text{O}_{\text{sw}}$  and temperature. UCDW is largely ventilated by waters coming from the North Atlantic (Tamsitt et al. 2017; Holzer et al. 2021), and  $\delta^{18}\text{O}_{\text{sw}}$  is higher in deep waters sourced in the North Atlantic than in those formed around Antarctica. Indeed North Atlantic surface waters undergo substantial evaporation as they travel north to their sinking sites (e.g. Worthington 1970), whereas AABW derives its elevated salinity from brine rejection, a process that causes little fractionation of seawater oxygen isotopes (Weiss et al. 1979). Furthermore, the glacial meltwater input at the Antarctic margins lowers the  $\delta^{18}\text{O}_{\text{sw}}$  of AABW (Toggweiler and Samuels 1995b), increasing the  $\delta^{18}\text{O}_{\text{sw}}$  contrast between AABW and NADW. In the present day, North Atlantic deep waters are also warmer than AABW and the deep vertical temperature gradient offsets the impact of the  $\delta^{18}\text{O}_{\text{sw}}$  difference on  $\delta_c$ , leading to relatively uniform deep ocean  $\delta_c$ . In contrast during the LGM, deep temperatures may have been more uniform (Adkins et al. 2002) likely allowing a  $\delta_c$  maximum to emerge at mid-depths.

The reconstructed profiles employing the modern North Pacific fractions (Fig. 4b) and the chosen end-members (Table 3) are shown as dashed lines in Fig. 4c.

We find that the reconstructed profile for the Holocene matches the deep data reasonably well; the mismatches at intermediate depths can largely be explained by the tendency of the Herguera et al. (2010) dataset to over-sample

(with respect to the basin mean) AAIW and UCDW at these depths (Supplementary Figures S3 and S4) and the influence of the subtropical gyre at the shallowest sites. We may similarly expect these spatial sampling biases to persist at the LGM, however removing the data from sites below 800 m [below which we expect the influence of the subtropical gyre to be minimal] results in an identical  $\delta_c$  profile, indicating the steep  $\delta_c$  gradient in the intermediate depths at the LGM persists once the influence of the subtropical gyre is removed. By contrast, the reconstructed LGM profile fails to reconstruct the glacial data and capture the mid-depth maximum and associated vertical gradients. Modifying the glacial  $\delta_c$  end-member values over reasonable ranges [by up to 5 times the observed difference] yields the same conclusion: using the modern water fractions, it is not possible to reproduce the shape of the glacial  $\delta_c$  profile. This implies that a change in water fractions (i.e., a change in circulation and mixing) is required to explain the glacial  $\delta_c$  observations.

To showcase a possible change in water fractions that would be compatible with observations, we construct idealized profiles of water fractions for the North Pacific at LGM (Fig. 5a). These idealized profiles are guided by four hypotheses. First, we presume that NPIW was expanded and overwhelmingly dominant at intermediate depths, influencing ocean properties down to about 2 km (Rae et al. 2020; Matsumoto et al. 2002; Keigwin 1998; Herguera et al. 2010; Struve et al. 2022). Second, we expect that glacial AAIW was shallower than today (Ronge et al. 2015) and therefore largely absent from the deep North Pacific. Consistent with this expectation, the LGM  $\delta_c$  of core *SO213\_84\_2-1* at 972 m depth in the South Pacific, corresponding to glacial AAIW (Ronge et al. 2015), is around 0.25 ‰ heavier than the mean  $\delta_c$  at the same depth in our LGM North Pacific compilation. We thus discard the AAIW end-member for this analysis (i.e. we set the AAIW fraction to zero). Third, we hypothesize that the peak UCDW fractions were situated about 400 m (minus LGM sea level change) deeper than today. This downward shift is suggested by the glacial  $\delta_c$  observations overlain on the estimated modern UCDW fraction (Fig. 6). Finally, guided by observations (Fig. 4c) and theory (Ferrari et al. 2014), we presume the deep Pacific Ocean to be strongly layered at LGM, such that each water mass occupies virtually all the North Pacific volume within its core depth range.

Combined with the end-member values of Table 3, the idealized profiles of water fractions in Fig. 5a yield a reconstructed glacial  $\delta_c$  profile that is roughly consistent with the observations deeper than 1 km (Fig. 5b). The slight overestimation of the mid-depth maximum is consistent with overestimation of the peak UCDW fraction, which was set to 1 over 2.2–3 km depth, an unrealistically high value given erosion by vertical mixing of the UCDW signature as it spreads northward. Still, much

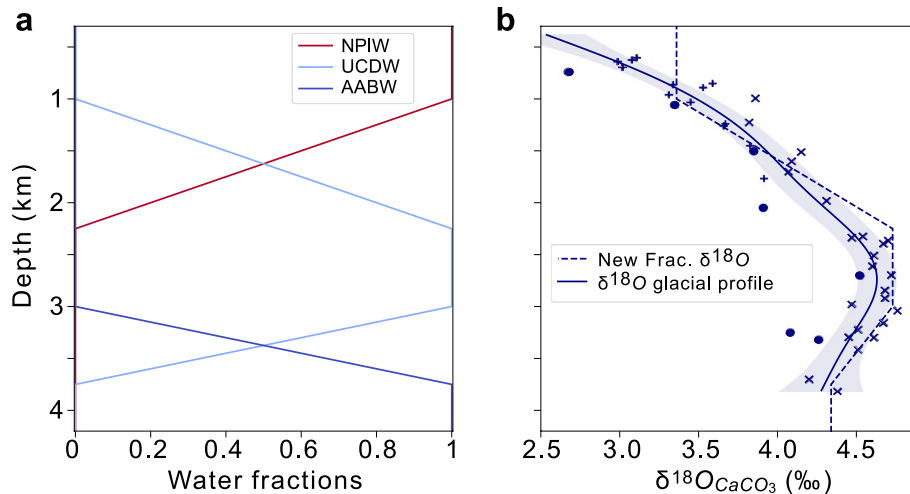


**Fig. 5** (a) shows idealized fractions for the glacial North Pacific (20–55°N) as a function of depth. Red is NPIW, light blue is UCDW and navy blue is AABW. In (b), we show the glacial  $\delta_c$  data and GAM fit (solid line and 95% confidence interval shaded) as presented in Fig. 4c, together with the reconstructed profile using the idealized

water fractions (dashed line). Sediment cores published by Keigwin (1998) are represented by crosses; the ones from Matsumoto et al. (2002), represented by circles; and the ones from Herguera et al. (2010), represented by plus signs

larger mid-depth UCDW fractions than the modern estimates (see Fig. 6) are necessary to reproduce the observed mid-depth bulge in glacial  $\delta_c$ —unless our end-member values grossly underestimate the source water-mass contrasts. This analysis thus bolsters the hypothesis of a stronger water-mass layering in the glacial deep North Pacific than today, presumably caused by reduced vertical diffusion or increased isopycnal diffusion or both.

### 4.3 Geothermal heat hypothesis

We asserted that the mid-depth maximum in  $\delta_c$  apparent in the LGM North Pacific data is too large to be explained by pressure-driven increase of in-situ temperature. However, the  $\sim 0.3\text{‰}$  difference we observe between 3 and 4 km depth (Figs. 4c and 6) could be driven, in theory (Marchitto et al. 2014), by a  $\sim 1.5\text{ °C}$  temperature increase from 3 to 4 km depth. If the abyssal Pacific was strongly stratified in salinity, such a temperature inversion could have existed without destabilizing the water column. The difference in absolute salinity between 4 and 3 km depth would need to exceed 0.33 g/kg (taking absolute salinity and conservative temperature at 4 km to be near 36 g/kg and 0.5 °C, respectively), about 17 times the present-day difference. Given that dense waters formed around Antarctica and in the high-latitude Atlantic were close to freezing point at LGM (Adkins et al. 2002), geothermal heating is the only possible source of this hypothetical abyssal heat reservoir (see Adkins et al. 2005).

Several considerations cast doubt on the ability of geothermal heating to explain, alone, the observed mid-depth maximum in glacial  $\delta_c$ . First, a 1.5 °C temperature excess at 4 km relative to 3 km requires a substantial (at least three-fold) increase in the residence time of Pacific bottom waters (deeper than 4 km) compared to today, and an even larger increase in the vertical geothermal heat gradient. Indeed it is estimated that present-day geothermal heating drives less than 0.5 °C warming in North Pacific waters deeper than 4 km, and about half this warming at 3 km depth (Adcroft et al. 2001; Emile-Geay and Madec 2009). Proxy estimates of Pacific abyssal flows (McCave et al. 2008) and

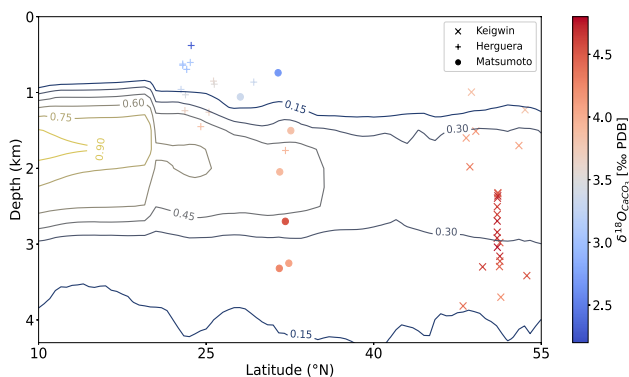


**Fig. 6** The  $\delta_c$  glacial data from our compilation is shown by shaded symbols, as a function of the latitude and water depth of each core. Crosses denote data from Keigwin (1998), plus signs data from Herguera et al. (2010) and circles data from Matsumoto et al. (2002). Contours show the zonally averaged UCDW fraction as estimated for the modern state

radiocarbon estimates (Rafter et al. 2022) do not suggest such a large residence time of the glacial Pacific bottom waters. In addition, the mid-depth maximum in  $\delta_c$  appears to be larger in the southwestern Pacific (Table 3) than in the North Pacific (4c), whereas geothermal heating is expected to cause abyssal warming that increases from south to north (Adcroft et al. 2001; Emile-Geay and Madec 2009). Hence, we consider it highly unlikely that geothermal heating can be the primary cause of the increase in abyssal to mid-depth  $\delta_c$ . Nonetheless, we cannot exclude that the imprint of geothermal heating on Pacific abyssal temperatures was larger than today, and that it contributes to increase the apparent influence of isopycnal diffusion from the south in the mid-depths.

## 5 Discussion

### 5.1 Vertical and lateral influences on Pacific mid-depths

Our analysis of modern tracer distributions, especially  $\delta^{18}\text{O}_{\text{sw}}$  from LeGrande and Schmidt (2006), and sediment archives of LGM  $\delta_c$  (Keigwin 1998; Matsumoto et al. 2002; Herguera et al. 2010), indicates that mid-depth (1.5–3 km) Pacific waters are not merely a mixture of waters lying below and above. A sizeable influence from Southern Ocean UCDW on Pacific mid-depths is inferred. This south-to-north isopycnal ventilation pathway is theoretically compatible with net southward volume transport at these depths (Fig. 1a), since strong isopycnal diffusion could overwhelm the influence of the overturning (Naveira Garabato et al. 2017). However, the estimated percentage influence of UCDW on the mid-depth North Pacific in the modern (Fig. 3c) and glacial (Fig. 5a) states advocates for weak vertical diffusion and overturning in this layer (Fig. 1b). We thus propose that relatively weak overturning allows isopycnal diffusion and recirculation to emerge as the primary communication pathway between Pacific mid-depths and surrounding oceans, in accord with a recent inverse model analysis (Holzer et al. 2021).

Beyond these common characteristics, the glacial and modern states appear to differ in important ways. In particular, the deep North Pacific may have been more strongly layered at LGM than it is today. Increased layering could arise from one or a combination of the following: (i) larger contrasts in source (end-member) water masses, (ii) increased isopycnal diffusion at mid-depths, and (iii) reduced vertical diffusion. More efficient isopycnal communication between Southern Ocean and North Pacific mid-depths in the glacial state could have contributed to maintain a more distinct water-mass signature at these depths. However it is not clear why isopycnal diffusion rates should have been much larger at LGM; this scenario would imply a widespread increase

in mesoscale eddy energy or decrease in mixing suppression by mean flows (Groeskamp et al. 2020; Abernathey et al. 2022). On the other hand, an increase in water-mass and density contrasts, together with reduced vertical mixing, appear to be plausible. Indeed, large LGM Antarctic sea ice seasonality (Crosta et al. 2022) is expected to strengthen the salinity contrast between bottom and intermediate waters (Ferrari et al. 2014; Haumann et al. 2016; Galbraith and de Lavergne 2019), potentially contributing to strong salinity-based stratification in the deep North Pacific (Adkins et al. 2002). In turn, increased stratification could have reduced vertical mixing rates, since vertical diffusivity is inversely proportional to vertical density gradient for a given power input to mixing (Osborn 1980).

### 5.2 Evidence from carbon isotopes

Carbon isotope observations provide some independent support for our interpretations of modern and glacial Pacific ventilation. In Fig. 7, we show the dominating end-member (as diagnosed in Sect. 3) and the zonally averaged radiocarbon distribution ( $\Delta^{14}\text{C}$ , from de Lavergne et al. (2017)) overlain with contours of the UCDW fraction, within the modern main Pacific. The  $\Delta^{14}\text{C}$  minimum is located at mid-depths between 30 and 45°N (Fig. 7b). The fact that this minimum is not located further north (i.e., further away from the southern sources of ventilation) concurs with the inferred upwelling of abyssal tracers in the subarctic Pacific. The latitudinal position of the  $\Delta^{14}\text{C}$  minimum appears to lie at the junction between the declining influence of UCDW towards the north, and the rising influence of AABW in the subarctic Pacific, as illustrated by the dominant water-mass distribution shown in Fig. 7a. What causes the rise of the AABW fraction and associated upwelling of tracers in the subarctic Pacific remains unknown, however. Potential causes include high vertical mixing, low isopycnal mixing and wind-driven uplifting (Toggweiler et al. 2019; Sigman et al. 2021).

In the cores that we used for the analysis of oxygen isotopes, the carbon isotopic ratio  $\delta^{13}\text{C}$  of benthic foraminifera was also measured. Although  $\delta^{13}\text{C}$  is not conservative since remineralization of organic matter lowers the ratio (Duplessy et al. 1988), it provides a source of information complementary to  $\delta_c$ . In Fig. 8, we show both the modern and glacial  $\delta^{13}\text{C}$  from the same cores that we used in Sect. 4. In the modern ocean,  $\delta^{13}\text{C}$  increases from 2.5 to 4 km depth, suggesting an older water mass at mid-depths than in the abyss. In the glacial ocean,  $\delta^{13}\text{C}$  exhibits a very different shape, with a minimum centred near 2.5 km depth, similar to the depth of the  $\delta_c$  maximum (Figs. 4c and 5b). This shape is qualitatively consistent with a relatively isolated mid-depth layer, sandwiched between younger AABW and expanded NPIW. Additionally, the differences in glacial  $\delta^{13}\text{C}$  between the dataset from the

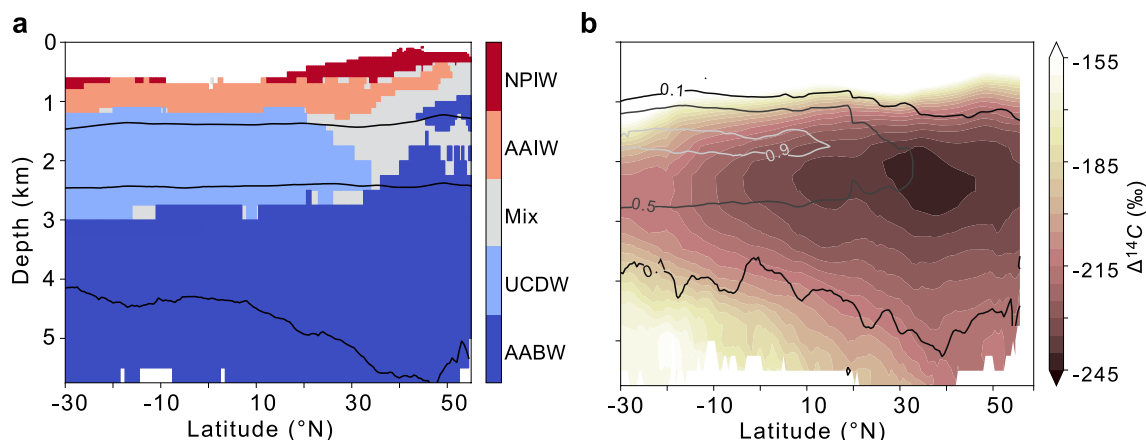


**Fig. 7** The dominating zonally averaged water fraction in the main Pacific is shaded in (a). A fraction is defined as dominant when superior to the sum of the other three. Grey shading indicates Where no fraction dominates (“Mix” zone). The characteristic isopycnals of the UCDW and AABW end-members are shown as black curves.

In (b), the zonal mean modern  $\Delta^{14}\text{C}$  distribution is shaded, and the zonal mean UCDW fraction is contoured. This figure illustrates that the radiocarbon minimum is located at the end of the UCDW tongue, near the “Mix” zone, where ventilation by isopycnal diffusion and diapycnal diffusion appears to be weakest

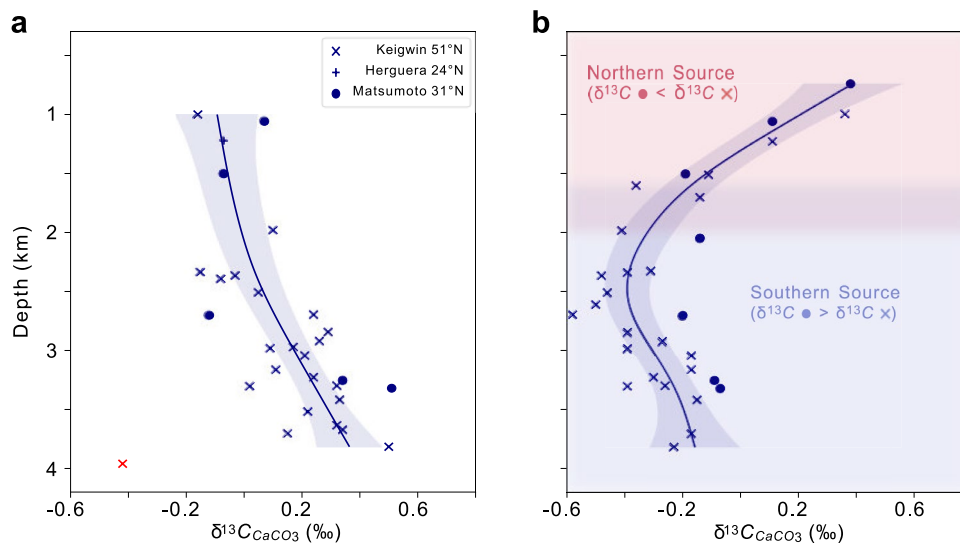


**Fig. 8** (a) Shows the modern  $\delta^{13}\text{C}$  values from our North Pacific compilation as a function of water depth. (b) Shows the equivalent for the LGM. In both panels, the data have been fitted with a GAM (dashed curves; 95% confidence interval is shaded). In (a), the deepest core (*Vinogr GGC-17\_2*, in red) was left out of the GAM calculation because of the large anomaly relative to the other modern values. In (b), light blue shading indicates a southern ventilation source,

while red shading indicates a northern source, as deduced from the geographical  $\delta^{13}\text{C}$  gradients (i.e. the differences between datasets of Keigwin (1998) and Matsumoto et al. (2002)). Data from Keigwin (1998) are marked with crosses, from Matsumoto et al. (2002) with circles, and from Herguera et al. (2010) with plus signs (only one  $\delta^{13}\text{C}$  value is available from the latter study, in (a)). In (a), the latitude indicated next to the name of the authors corresponds to the average latitude of each study’s cores

coast of Japan (Matsumoto et al. 2002) and that near the Bering Strait (Keigwin 1998) (see Fig. 5a) corroborate the notion that ventilation was dominantly south-to-north deeper than 1.5–2 km, and dominantly north-to-south at intermediate depths (see shading in Fig. 8b). Indeed, when moving toward the north (from circles to crosses

in Fig. 8b),  $\delta^{13}\text{C}$  becomes lighter (respectively heavier) in the deeper (respectively shallower) part of the water column. Furthermore, the vertical gradient between mid-depths (2–3 km) and deeper waters also appears to increase toward the north; although uncertain, this pattern

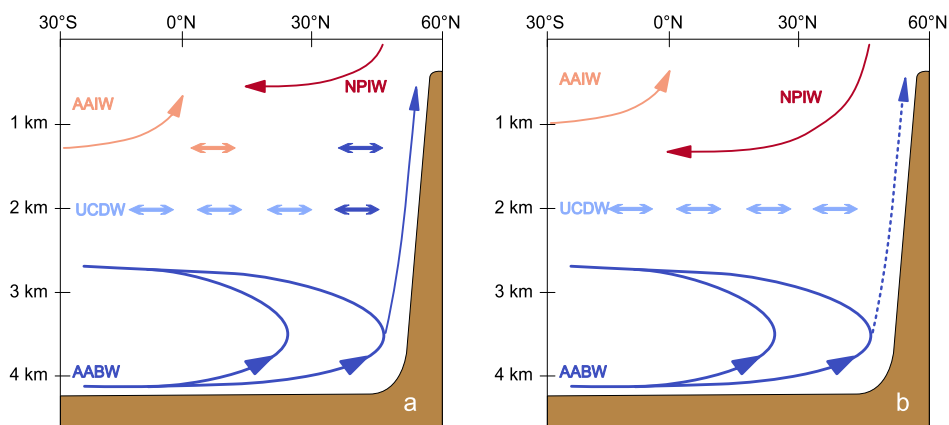


**Fig. 9** Proposed modern (a) and glacial (b) Pacific ocean circulation regimes. Curved arrows denote major circulation branches while double-headed straight arrows denote isopycnal diffusion and recirculation. In the glacial state, an expansion of NPIW to the detriment of AAIW may have taken place at intermediate depths, while stronger stratification in deeper layers may have decreased the upwelling of abyssal tracers in the subarctic Pacific leading to an increased northward penetration of UCDW. Note that the inferred slight deepening of the UCDW influence at LGM is not represented on the schematic for simplicity; this deepening probably results from the other circulation changes

### 5.3 Implications for glacial carbon storage

Together, oxygen and carbon isotopes thus suggest increased layering of the different water masses in the North Pacific at the LGM relative to present. An increase in deep stratification probably reduced the upwelling of abyssal tracers, leading to the increased layering observed in the deep Pacific. This was possibly associated with stronger NPIW influence in the upper 1.5 km. The combined NPIW expansion and reduced AABW influence in the mid-depths of the subarctic Pacific would have resulted in a stronger and slightly deeper UCDW influence at mid-depths. These circulation changes are summarized in Fig. 9. Modern upwelling of abyssal tracers in the subarctic Pacific influences the tracer distributions at mid and intermediate depths, acting as an important return pathway for nutrients (Sarmiento et al. 2004; Holzer et al. 2021). A reduction in the upwelling of abyssal tracers at LGM would limit the return path of remineralized nutrients through the mid-depths which would thus reduce CO<sub>2</sub> outgassing from the surface. A host of biogeochemical tracers suggest a reduction in the supply of nutrients and carbon to the surface of the subarctic Pacific during the LGM (Jaccard et al. 2009; Ren et al. 2015; Gray et al. 2018), despite climate models indicating a substantial increase in wind-driven upwelling within the region under glacial boundary conditions (Gray et al. 2018, 2020). This can be explained by the reduced influence of AABW and increased influence of NPIW at intermediate depths (Fig. 9), which would have lowered the nutrient concentrations of the upwelling waters (Rae et al. 2020). Furthermore, the expansion of NPIW

provides a new-source of low-preformed nutrient water in the global ocean, providing a mechanism to lower atmospheric CO<sub>2</sub> (Rae et al. 2020). These changes are complementary and would work together to increase the efficiency of the biological pump: the expansion of NPIW lowers the ocean's preformed nutrient inventory, while reduced vertical mixing in the deep ocean would trap remineralized nutrient in the abyss. The proposed changes in ventilation thus likely imply an increase in oceanic carbon storage during glacial times relative to present.

Over deglaciation, upwelling from the abyssal subarctic Pacific appears to have increased around the onset of the Bolling-Allerod, roughly coeval with onset of modern rates of NADW formation (Galbraith et al. 2007), bringing carbon-rich deepwaters to the surface in the subarctic Pacific and outgassing CO<sub>2</sub> to the atmosphere (Gray et al. 2018).

## 6 Conclusion

We analysed the distribution of quasi-conservative tracers, including oxygen isotopes in seawater and benthic foraminifera, to constrain ventilation patterns in the modern and glacial Pacific Ocean. The analysis supports a crucial role for isopycnal diffusion in the ventilation of Pacific mid-depths (1.5–3 km). However, substantial vertical tracer transport from the abyss to the upper ocean appears to overwhelm this isopycnal influence in the modern subarctic Pacific (north of about 40°N). Isotopes of benthic foraminifera ( $\delta^{18}\text{O}$  and  $\delta^{13}\text{C}$ ) from the North Pacific suggest a stronger layering of the deep ocean during the LGM than at present, including a possible suppression of the subarctic bottom-to-surface tracer upwelling. A reduction in vertical mixing linked to increased



stratification in the deep North Pacific, and an expansion of NPIW, may have contributed to these differences. Overall, the inferred changes in ventilation would imply that North Pacific deep waters were more isolated and more carbon rich at LGM than they are today. Further work is required to better understand the drivers of subarctic Pacific upwelling, and to better constrain the LGM North Pacific water-mass structure and its implications for deep ocean carbon storage.

## 6.1 Supplementary information

This article has five figures in supplementary materials and a csv file containing the North Pacific compilation data. The water fractions and associated error datasets are accessible at: <https://doi.org/10.5281/zenodo.8183224>.

**Supplementary Information** The online version contains supplementary material available at <https://doi.org/10.1007/s00382-023-06910-8>.

**Acknowledgements** We thank Claire Waelbroeck, Elisabeth Michel, Nathaëlle Bouttes, James Rae and Kazuyo Tachikawa for helpful discussions. We are grateful to two anonymous reviewers for their thoughtful and constructive comments. DMR is supported by CNRS and VU Amsterdam.

**Funding** Financial support was provided by a thesis grant from the French Alternative Energies and Atomic Energy Commission (CEA), the French national LEFE programme through the ROOF project, and ANR grant CARBCOMP.

**Data availability** The water fractions and associated error datasets are accessible at <https://doi.org/10.5281/zenodo.8183224>.

## Declarations

**Conflict of interest** The authors have no competing interests to declare that are relevant to the content of this article.

**Open Access** This article is licensed under a Creative Commons Attribution 4.0 International License, which permits use, sharing, adaptation, distribution and reproduction in any medium or format, as long as you give appropriate credit to the original author(s) and the source, provide a link to the Creative Commons licence, and indicate if changes were made. The images or other third party material in this article are included in the article's Creative Commons licence, unless indicated otherwise in a credit line to the material. If material is not included in the article's Creative Commons licence and your intended use is not permitted by statutory regulation or exceeds the permitted use, you will need to obtain permission directly from the copyright holder. To view a copy of this licence, visit <http://creativecommons.org/licenses/by/4.0/>.

## References

- Abernathy R, Gnanadesikan A, Pradal MA et al (2022) Chapter 9— isopycnal mixing. In: Meredith M, Naveira Garabato A (eds) Ocean mixing. Elsevier, Amsterdam, pp 215–256. <https://doi.org/10.1016/B978-0-12-821512-8.00016-5>
- Adcroft A, Scott JR, Marotzke J (2001) Impact of geothermal heating on the global ocean circulation. *Geophys Res Lett* 28(9):1735–1738. <https://doi.org/10.1029/2000GL012182>
- Adkins JF (2013) The role of deep ocean circulation in setting glacial climates. *Paleoceanography* 28(3):539–561. <https://doi.org/10.1002/palo.20046>
- Adkins JF, McIntyre K, Schrag DP (2002) The salinity, temperature, and  $\delta^{18}\text{O}$  of the glacial deep ocean. *Science* 298(5599):1769–1773. <https://doi.org/10.1126/science.1076252>
- Adkins JF, Ingersoll AP, Pasquero C (2005) Rapid climate change and conditional instability of the glacial deep ocean from the thermobaric effect and geothermal heating. *Quatern Sci Rev* 24(5):581–594. <https://doi.org/10.1016/j.quascirev.2004.11.005>
- Anderson LA, Sarmiento JL (1994) Redfield ratios of remineralization determined by nutrient data analysis. *Global Biogeochem Cycles* 8(1):65–80. <https://doi.org/10.1029/93GB03318>
- Augustin L, Barbante C, Barnes PRF et al (2004) Eight glacial cycles from an antarctic ice core. *Nature* 429(6992):623–628. <https://doi.org/10.1038/nature02599>
- Broecker WS, Takahashi T, Takahashi T (1985) Sources and flow patterns of deep-ocean waters as deduced from potential temperature, salinity, and initial phosphate concentration. *J Geophys Res Oceans* 90(C4):6925–6939. <https://doi.org/10.1029/JC090iC04p06925>
- Crosta X, Kohfeld KE, Bostock HC et al (2022) Antarctic sea ice over the past 130 000 years—part 1: a review of what proxy records tell us. *Climate Past* 18(8):1729–1756. <https://doi.org/10.5194/cp-18-1729-2022>
- Curry W, Oppo D (2005) Glacial water mass geometry and the distribution of  $\delta^{13}\text{C}$  of  $\Sigma \text{CO}_2$  in the western atlantic ocean. *Paleoceanography* 20:859–869. <https://doi.org/10.1029/2004PA001021>
- de Lavergne C, Madec G, Roquet F et al (2017) Abyssal ocean overturning shaped by seafloor distribution. *Nature* 551(7679):181–186. <https://doi.org/10.1038/nature24472>
- de Lavergne C, Groeskamp S, Zika J et al (2022) Chapter 3—the role of mixing in the large-scale ocean circulation. In: Meredith M, Naveira Garabato A (eds) Ocean Mixing. Elsevier, Amsterdam, pp 35–63. <https://doi.org/10.1016/B978-0-12-821512-8.00010-4>
- Duplessy JC, Shackleton NJ, Fairbanks RG et al (1988) Deep water source variations during the last climatic cycle and their impact on the global deep water circulation. *Paleoceanography* 3(3):343–360. <https://doi.org/10.1029/PA003i003p00343>
- Emile-Geay J, Madec G (2009) Geothermal heating, diapycnal mixing and the abyssal circulation. *Ocean Sci* 5(2):203–217. <https://doi.org/10.5194/os-5-203-2009>
- Ferrari R, Jansen MF, Adkins JF et al (2014) Antarctic sea ice control on ocean circulation in present and glacial climates. *Proc Natl Acad Sci* 111(24):8753–8758. <https://doi.org/10.1073/pnas.1323922111>
- Galbraith E, de Lavergne C (2019) Response of a comprehensive climate model to a broad range of external forcings: relevance for deep ocean ventilation and the development of late cenozoic ice ages. *Clim Dyn* 52(1):653–679. <https://doi.org/10.1007/s00382-018-4157-8>
- Galbraith ED, Jaccard SL, Pedersen TF et al (2007) Carbon dioxide release from the north pacific abyss during the last deglaciation. *Nature* 449(7164):890–893. <https://doi.org/10.1038/nature06227>
- Ganachaud A, Wunsch C (2000) Improved estimates of global ocean circulation, heat transport and mixing from hydrographic data. *Nature* 408(6811):453–457. <https://doi.org/10.1038/35044048>
- Gouretski V, Koltermann KP (2004) Woce global hydrographic climatology. *Berichte des BSH* 35:1–52
- Gray WR, Rae JWB, Wills RCJ et al (2018) Deglacial upwelling, productivity and  $\text{CO}_2$  outgassing in the north pacific ocean. *Nat Geosci* 11(5):340–344. <https://doi.org/10.1038/s41561-018-0108-6>
- Gray WR, Wills RCJ, Rae JWB et al (2020) Wind-driven evolution of the north pacific subpolar gyre over the last deglaciation. *Geophys Res Lett* 47(6):e2019GL086328. <https://doi.org/10.1029/2019GL086328>

- Groeskamp S, LaCasce JH, McDougall TJ et al (2020) Full-depth global estimates of ocean mesoscale eddy mixing from observations and theory. *Geophys Res Lett* 47(18):e2020GL089425. <https://doi.org/10.1029/2020GL089425>
- Haumann FA, Gruber N, Münnich M et al (2016) Sea-ice transport driving southern ocean salinity and its recent trends. *Nature* 537(7618):89–92. <https://doi.org/10.1038/nature19101>
- Hautala SL (2018) The abyssal and deep circulation of the northeast Pacific basin. *Prog Oceanogr* 160:68–82. <https://doi.org/10.1016/j.pocean.2017.11.011>
- Herguera J, Herbert T, Kashgarian M et al (2010) Intermediate and deep water mass distribution in the Pacific during the last glacial maximum inferred from oxygen and carbon stable isotopes. *Quatern Sci Rev* 29(9):1228–1245. <https://doi.org/10.1016/j.quascirev.2010.02.009>
- Herguera JC, Jansen E, Berger WH (1992) Evidence for a bathyal front at 2000-m depth in the glacial Pacific, based on a depth transect on Ontong Java plateau. *Paleoceanography* 7(3):273–288. <https://doi.org/10.1029/92PA00869>
- Holzer M, DeVries T, de Lavergne C (2021) Diffusion controls the ventilation of a Pacific shadow zone above abyssal overturning. *Nat Commun* 12(1):4348. <https://doi.org/10.1038/s41467-021-24648-x>
- Jaccard S, Galbraith E, Sigman D et al (2009) Subarctic Pacific evidence for a glacial deepening of the oceanic respired carbon pool. *Earth Planet Sci Lett* 277(1):156–165. <https://doi.org/10.1016/j.epsl.2008.10.017>
- Jackett DR, McDougall TJ (1997) A neutral density variable for the world's oceans. *J Phys Oceanogr* 27(2):237–263. [https://doi.org/10.1175/1520-0485\(1997\)027<0237:ANDVFT>2.0.CO;2](https://doi.org/10.1175/1520-0485(1997)027<0237:ANDVFT>2.0.CO;2)
- Johnson GC (2008) Quantifying Antarctic bottom water and North Atlantic deep water volumes. *J Geophys Res Oceans*. <https://doi.org/10.1029/2007JC004477>
- Kawasaki T, Hasumi H, Tanaka Y (2021) Role of tide-induced vertical mixing in the deep Pacific ocean circulation. *J Oceanogr* 77(2):173–184. <https://doi.org/10.1007/s10872-020-00584-0>
- Keigwin LD (1998) Glacial-age hydrography of the far northwest Pacific ocean. *Paleoceanography* 13(4):323–339. <https://doi.org/10.1029/98PA00874>
- Key RM (2004) A global ocean carbon climatology: results from global data analysis project (GLODAP). *Global Biogeochem Cycles* 18(4):GB4031. <https://doi.org/10.1029/2004GB002247>
- LeGrande AN, Schmidt GA (2006) Global gridded data set of the oxygen isotopic composition in seawater. *Geophys Res Lett*. <https://doi.org/10.1029/2006GL026011>
- Lund DC, Adkins JF, Ferrari R (2011) Abyssal Atlantic circulation during the last glacial maximum: constraining the ratio between transport and vertical mixing. *Paleoceanography*. <https://doi.org/10.1029/2010PA001938>
- Marchitto T, Curry W, Lynch-Stieglitz J et al (2014) Improved oxygen isotope temperature calibrations for cosmopolitan benthic foraminifera. *Geochim Cosmochim Acta* 130:1–11. <https://doi.org/10.1016/j.gca.2013.12.034>
- Matsumoto K, Oba T, Lynch-Stieglitz J et al (2002) Interior hydrography and circulation of the glacial Pacific ocean. *Quatern Sci Rev* 21(14):1693–1704. [https://doi.org/10.1016/S0277-3791\(01\)00142-1](https://doi.org/10.1016/S0277-3791(01)00142-1)
- McCave I, Carter L, Hall I (2008) Glacial–interglacial changes in water mass structure and flow in the SW Pacific Ocean. *Quatern Sci Rev* 27(19):1886–1908. <https://doi.org/10.1016/j.quascirev.2008.07.010>
- McDougall TJ, Barker PM (2011) Getting started with Teos—10 and the Gibbs seawater (gsw) oceanographic toolbox. SCOR/IAPSO WG127, ISBN 978-0-646-55621-5
- McDougall TJ, Jackett DR, Millero FJ et al (2012) A global algorithm for estimating absolute salinity. *Ocean Sci* 8(6):1123–1134. <https://doi.org/10.5194/os-8-1123-2012>
- Moreno AR, Larkin AA, Lee JA et al (2022) Regulation of the respiration quotient across ocean basins. *AGU Adv*. <https://doi.org/10.1029/2022AV000679>
- Moy AD, Howard WR, Gagan MK (2006) Late quaternary palaeoceanography of the circumpolar deep water from the south Tasman rise. *J Quatern Sci* 21:763–777. <https://doi.org/10.1002/jqs.1067>
- Naveira Garabato AC, MacGilchrist GA, Brown PJ et al (2017) High-latitude ocean ventilation and its role in Earth's climate transitions. *Philos Trans R Soc A Math Phys Eng Sci* 375(2102):20160324. <https://doi.org/10.1098/rsta.2016.0324>
- Okazaki Y, Timmermann A, Menviel L et al (2010) Deepwater formation in the North Pacific during the last glacial termination. *Science* 329(5988):200–204. <https://doi.org/10.1126/science.1190612>
- Olsen A, Key RM, van Heuven S et al (2016) The global ocean data analysis project version 2 (GLODAPV2)—an internally consistent data product for the world ocean. *Earth Syst Sci Data* 8(2):297–323. <https://doi.org/10.5194/essd-8-297-2016>
- Osborn TR (1980) Estimates of the local rate of vertical diffusion from dissipation measurements. *J Phys Oceanogr* 10(1):83–89. [https://doi.org/10.1175/1520-0485\(1980\)010<0083:EOTLRO>2.0.CO;2](https://doi.org/10.1175/1520-0485(1980)010<0083:EOTLRO>2.0.CO;2)
- Rae JWB, Broecker W (2018) What fraction of the Pacific and Indian oceans' deep water is formed in the southern ocean? *Biogeosciences* 15(12):3779–3794. <https://doi.org/10.5194/bg-15-3779-2018>
- Rae JWB, Sarnthein M, Foster GL et al (2014) Deep water formation in the north Pacific and deglacial CO<sub>2</sub> rise. *Paleoceanography* 29(6):645–667. <https://doi.org/10.1002/2013PA002570>
- Rae JWB, Gray WR, Wills RCJ et al (2020) Overturning circulation, nutrient limitation, and warming in the glacial North Pacific. *Sci Adv* 6(50):eabd1654. <https://doi.org/10.1126/sciadv.abd1654>
- Rafter PA, Gray WR, Hines SK et al (2022) Global reorganization of deep-sea circulation and carbon storage after the last ice age. *Sci Adv*. <https://doi.org/10.1126/sciadv.abq5434>
- Ren H, Studer AS, Serno S et al (2015) Glacial-to-interglacial changes in nitrate supply and consumption in the Subarctic North Pacific from microfossil-bound n isotopes at two trophic levels. *Paleoceanography* 30(9):1217–1232. <https://doi.org/10.1002/2014PA002765>
- Ronge TA, Steph S, Tiedemann R et al (2015) Pushing the boundaries: glacial/interglacial variability of intermediate and deep waters in the Southwest Pacific over the last 350,000 years. *Paleoceanography* 30(2):23–38. <https://doi.org/10.1002/2014PA002727>
- Sarmiento JL, Gruber N, Brzezinski MA et al (2004) High-latitude controls of thermocline nutrients and low latitude biological productivity. *Nature* 427(6969):56–60. <https://doi.org/10.1038/nature02127>
- Sigman DM, Boyle EA (2000) Glacial/interglacial variations in atmospheric carbon dioxide. *Nature* 407(6806):859–869. <https://doi.org/10.1038/35038000>
- Sigman DM, Fripiat F, Studer AS et al (2021) The southern ocean during the ice ages: a review of the antarctic surface isolation hypothesis, with comparison to the North Pacific. *Quatern Sci Rev* 254(106):732. <https://doi.org/10.1016/j.quascirev.2020.106732>
- Stewart AL (2017) Mixed up at the sea floor. *Nature* 551(7679):178–179. <https://doi.org/10.1038/551178b>
- Struve T, Wilson DJ, Hines SKV et al (2022) A deep Tasman outflow of Pacific waters during the last glacial period. *Nat Commun* 13(1):3763. <https://doi.org/10.1038/s41467-022-31116-7>
- Talley LD (1993) Distribution and formation of North Pacific intermediate water. *J Phys Oceanogr* 23(3):517–537. [https://doi.org/10.1175/1520-0485\(1993\)023<0517:DAFONP>2.0.CO;2](https://doi.org/10.1175/1520-0485(1993)023<0517:DAFONP>2.0.CO;2)

- Talley LD (2013) Closure of the global overturning circulation through the Indian, Pacific, and southern oceans: schematics and transports. *Oceanography* 26(1):80–97
- Tamsitt V, Drake HF, Morrison AK et al (2017) Spiraling pathways of global deep waters to the surface of the southern ocean. *Nat Commun* 8(1):172. <https://doi.org/10.1038/s41467-017-00197-0>
- Toggweiler J, Samuels B (1995) Effect of drake passage on the global thermohaline circulation. *Deep Sea Res I* 42(4):477–500. [https://doi.org/10.1016/0967-0637\(95\)00012-U](https://doi.org/10.1016/0967-0637(95)00012-U)
- Toggweiler JR, Samuels B (1995) Effect of sea ice on the salinity of Antarctic bottom waters. *J Phys Oceanogr* 25(9):1980–1997. [https://doi.org/10.1175/1520-0485\(1995\)025<1980:EOSIOT>2.CO;2](https://doi.org/10.1175/1520-0485(1995)025<1980:EOSIOT>2.CO;2)
- Toggweiler JR, Druffel ERM, Key RM et al (2019) Upwelling in the ocean basins north of the ACC: 1. On the upwelling exposed by the surface distribution of  $\Delta 14c$ . *J Geophys Res Oceans* 124(4):2591–2608. <https://doi.org/10.1029/2018JC014794>
- Warren BA (1973) Transpacific hydrographic sections at lats. 43°s and 28°s: the scorpia expedition—II. Deep water. *Deep-Sea Res Oceanogr Abstr* 20(1):9–38. [https://doi.org/10.1016/0011-7471\(73\)90040-5](https://doi.org/10.1016/0011-7471(73)90040-5)
- Warren BA (1983) Why is no deep water formed in the North Pacific? *J Mar Res* 41:327–347. <https://doi.org/10.1357/002224083788520207>
- Weiss R, Östlund H, Craig H (1979) Geochemical studies of the Weddell sea. *Deep Sea Res Part A Oceanogr Res Pap* 26(10):1093–1120. [https://doi.org/10.1016/0198-0149\(79\)90059-1](https://doi.org/10.1016/0198-0149(79)90059-1)
- Wood SN (2011) Fast stable restricted maximum likelihood and marginal likelihood estimation of semiparametric generalized linear models. *J R Stat Soc Ser B (Stat Methodol)* 73(1):3–36. <https://doi.org/10.1111/j.1467-9868.2010.00749.x>
- Wood SN, Pya N, Säfken B (2016) Smoothing parameter and model selection for general smooth models. *J Am Stat Assoc* 111(516):1548–1563. <https://doi.org/10.1080/01621459.2016.1180986>
- Worthington L (1970) The Norwegian sea as a Mediterranean basin. *Deep-Sea Res Oceanogr Abstr* 17(1):77–84. [https://doi.org/10.1016/0011-7471\(70\)90088-4](https://doi.org/10.1016/0011-7471(70)90088-4)

**Publisher's Note** Springer Nature remains neutral with regard to jurisdictional claims in published maps and institutional affiliations.